HAL open science

Determination of mass transfer coefficients in high-pressure CO2-H2O flows in microcapillaries using a colorimetric method

Thomas Deleau, Jean-jacques Letourneau, Séverine Camy, Joelle Aubin, Fabienne Espitalier

To cite this version:

Thomas Deleau, Jean-jacques Letourneau, Séverine Camy, Joelle Aubin, Fabienne Espitalier. Determination of mass transfer coefficients in high-pressure CO2-H2O flows in microcapillaries using a colorimetric method. Chemical Engineering Science, 2022, 248 (Part B), pp.1-15/117161. 10.1016/j.ces.2021.117161 . hal-03364885

HAL Id: hal-03364885

https://imt-mines-albi.hal.science/hal-03364885

Submitted on 18 Oct 2021

HAL is a multi-disciplinary open access archive for the deposit and dissemination of scientific research documents, whether they are published or not. The documents may come from teaching and research institutions in France or abroad, or from public or private research centers.

L'archive ouverte pluridisciplinaire **HAL**, est destinée au dépôt et à la diffusion de documents scientifiques de niveau recherche, publiés ou non, émanant des établissements d'enseignement et de recherche français ou étrangers, des laboratoires publics ou privés.

Determination of mass transfer coefficients in high-pressure CO_2-H_2O flows in microcapillaries using a colorimetric method

T. Deleau [a,b], J-J. Letourneau [a], S. Camy [b], J. Aubin [b,*], F. Espitalier [a]

[a] Université de Toulouse, Mines Albi, Centre RAPSODEE UMR CNRS 5302, Campus Jarlard, Albi, France
[b] Université de Toulouse, Laboratoire de Génie Chimique, UMR CNRS 5503, INPT, Toulouse, France

- Mass transfer of CO_2 into a H_2O-rich phase at high pressure in a microreactor is studied.
- Volumetric k_La_L and local k_L mass transfer coefficients are determined.
- The influence of CO_2 and H_2O flow rates on the volumetric mass transfer coefficient is studied.
- k_La_L and k_L vary along the length of the microcapillary.

Keywords:
Mass transfer
High-pressure
Microfluidics
Two-phase flow
Colorimetric method

A B S T R A C T

This study presents a method for the experimental determination of the local volumetric mass transfer coefficient k_La_L in a high-pressure two-phase flow of water (H_2O) and carbon dioxide (CO_2) in a microcapillary using a colorimetric method. H_2O and CO_2 are fed continuously and co-axially injected at high-pressure (10 MPa) and moderate temperature (303 K) into a microcapillary. Under the flow conditions studied, a segmented flow of CO_2 in H_2O is formed. The CO_2 dissolves into the H_2O-rich phase, thereby reducing the pH to about 3.3, depending on the pressure and temperature. The pH of the H_2O-rich phase is determined over the entire length of the capillary using a pH sensitive indicator coupled with high-speed imaging and analysis. The concentration of CO_2 in the water-rich phase is deduced from this pH value using literature experimental data. The CO_2 concentration data and the unit-cell model, which has been modified to account for high pressure conditions, have then been used to determine the volumetric mass transfer coefficient, k_La_L, of CO_2 into the liquid phase along the entire length of the microreactor. The experimentally derived k_La_L ranges between 1 and 13 s^{-1}.

1. Introduction

The use of supercritical fluids (fluids under temperature and pressure conditions above those of their critical point) in liquid-fluid extraction (Conde-Hernández et al., 2017; Yousefi et al., 2019), multiphase reaction (Ou et al., 2019; Labauze et al., 2018), particle generation processes (Abuzar et al., 2018; Cheng et al., 2017) or even in analytical chemistry (DaSilva et al., 2020; Roy et al., 2020) is more and more widespread. Indeed, supercritical fluids have specific properties (i.e. liquid-like density and gas-like viscosity), which makes them just as, or even more effective than conventional solvents in many cases. Moreover, the use of supercritical CO_2 results in cleaner and more sustainable processes and products. Supercritical CO_2 processes typically involve multiple phases and the design of such processes requires knowledge of the thermodynamic properties of the different phases at high pressure and sometimes high temperature. These properties include, for example, mixing density and viscosity (at saturation or not), surface tension, as well as diffusion coefficients for transient processes. The acquisition of such data very often requires investment in specific equipment that can withstand high temperature and pressure conditions, but also long experimental campaigns (for saturated data, one measurement with conventional pressure-volume-temperature (PVT) devices takes approximately half a day). One solution to overcome these disadvantages of conventional PVT measurement methods is to use miniaturised devices such as microreactors. The typical size of a microreactor is about 10^4 times smaller than conventional apparatus and as a result the characteristic heat and mass transfer times, which are

* Corresponding author.
E-mail addresses: thomas.deleau@mines-albi.fr (T. Deleau), jean-jacques.letourneau@mines-albi.fr (J-J. Letourneau), severine.camy@ensiacet.fr (S. Camy), joelle.aubin@ensiacet.fr (J. Aubin), fabienne.espitalier@mines-albi.fr (F. Espitalier).

Nomenclature

a	specific surface area, m^{-1}
C	concentration, mol/m^3
D	diameter, m
K	overall mass transfer coefficient, m/s
k	local mass transfer coefficient, m/s
L	length,m
N	molar density flux, $mol/m^2/s$
p	pressure, Pa
Re	Reynolds number $\frac{UD\rho}{\mu}$
S	capillary cross section, m^2
T	temperature, K
U	velocity, m/s
V	volume, m^3
$\dot{V}$	volumetric flow rate, m^3/s
z	position in the capillary, m

Subscripts

B	bubble
cap	capillary
CO_2	carbon dioxide
F	fluid
H_2O	water
L	liquid
S	liquid slug
TP	two-phase

Superscripts

*	at equilibrium
~	mean value

proportional to the square of the characteristic length scale, are reduced by a factor of 10^8. This means that thermodynamic equilibria can be reached in just a few seconds, compared with several hours in conventional equipment. In addition, the use of small quantities of products reduces operating costs (in terms of both raw material and energy) and increases safety when toxic products are used.

Different kinds of pressure-resistant microreactors (which are compatible with the use of supercritical fluids) have been developed and reviewed (Marre et al., 2010). It is now possible to manufacture microreactors at low cost with various techniques, for example with silica capillaries (Macedo Portela da Silva et al., 2014) or polymer molding techniques (Martin et al., 2016). Supercritical microfluidics has been developed in various fields such as extraction (Assmann et al., 2012; Campos Domínguez and Gamse, 2016), organic chemistry (Verboom, 2009; Quitain et al., 2018), generation of nanomaterials (Arora et al., 2020; Jaouhari et al., 2020) or even for the acquisition of thermodynamic data (Liu et al., 2012; Klima and Braeuer, 2019; Gavoille et al., 2019).

Two-phase gas-liquid flows in microreactors have been widedly studied over the last 20 years and there is a wealth of information available in the literature (Haase et al., 2016; Sattari-Najafabadi et al., 2018). The first studies consisted in describing the different types of gas-liquid flow regimes depending on the operating conditions such as temperature, pressure and flow rates of each of the phases (Triplett et al., 1999; Akbar et al., 2002; Waelchli and Rudolf von Rohr, 2006; Marre et al., 2009; Blanch-Ojea et al., 2012; Martin et al., 2018). Several flow regimes are typically observed, including dispersed, bubbly, confined, slug, annular and churn flows. Among these flows, slug-flow, otherwise called "Taylor flow", is characterized by a highly regular sequence of liquid slugs and gas bubbles, with a large interfacial area. This flow is also characterized by flow recirculation in both the slug and bubble that leads to the enhancement of mass and heat transfer rates and process intensification (Luther et al., 2013; Peters et al., 2017).

In the litterature, several methods have been used to determine the volumetric mass transfer coefficients in two-phase segmented flow in microchannels at atmospheric pressure. These methods can be classified into three groups:

- Global experimental methods: Solute concentration in one of the phases is measured at the inlet and the outlet of the microreactor and is used to obtain an average volumetric mass transfer coefficient k_La_L over the entire length of the microreactor (Vandu et al., 2005; Yue et al., 2007; Ren et al., 2012).
- Online experimental methods: The gas dissolution is monitored in the microchannel by detecting changes in fluorescence intensity (Kuhn and Jensen, 2012), color (Dietrich et al., 2013), pressure drop (Yue et al., 2007; Ganapathy et al., 2014; Yao et al., 2017) or bubble size (Tan et al., 2012; Lefortier et al., 2012; Yao et al., 2014; Zhang et al., 2018). With online methods, k_La_L can be determined at different positions along the microcapillary.
- Numerical methods: The volumetric mass transfer coefficient is calculated using computational fluid dynamics to solve the Navier Stokes equation in the liquid phase and the convection-diffusion equation with a known value of the diffusion coefficient (van Baten and Krishna, 2004; Eskin and Mostowfi, 2012; Gupta et al., 2009). The gas is typically assumed to behave as an ideal gas.

Amongst the online methods mentioned above, the measurement of a change in size (volume) of gas bubbles has widely been used (Yao et al., 2014, 2017; Zhang et al., 2018). This method is well adapted at atmospheric pressure conditions since the bulk properties of the continuous phase, such as density, are not affected by the mixture variation and mass transfer can therefore be considered as unidirectional (from the dispersed phase to the continuous phase). This method is however far less suitable for the study of high-pressure two-phase flows where the thermodynamic mixing properties can vary greatly between the contacting zone of the fluids and the zone where thermodynamic equilibrium is reached. An example of such changes in fluid properties due to the transfer of species between phases is given in Macedo Portela da Silva et al. (2014). For a CO_2-$BMimPF_6$ system at 15 MPa and 308 K, the density and viscosity of the ionic liquid saturated with CO_2 are 1.7 times higher and 12 times smaller, respectively, than the pure ionic liquid at these same pressure and temperature conditions. Hence for high-pressure systems where there is significant mass transfer of species between phases, other measurement methods are required. Recently, Deleau et al. (2020) have presented a method for the experimental determination of local volumetric mass transfer coefficients k_La_L in a high-pressure (up to 10 MPa) two-phase flow of H_2O and CO_2 in a microcapillary. This method combines a thermodynamic model and Raman spectroscopy measurements to obtain CO_2 concentrations, which are used to calculate local k_La_L values. This method does not, however, enable information on the bubbles (e.g. surface area, velocity) to be obtained so it is not possible to evaluate the individual contributions of k_L and a_L to the volumetric mass transfer coefficient.

The objective of this work is to present an alternate method for the determination of volumetric mass transfer coefficient $k_L a_L$ in high pressure two-phase flows using a colorimetric method. This method has been adapted from that proposed by Andersson et al. (2018) and is based on the change in pH of a continuous H_2O-rich phase that is acidified by a dispersed phase (here a CO_2-rich phase). This method also enables the specific surface area (here defined as the bubble surface area divided by the volume of the liquid slug since the mass balance is performed in the liquid phase only) available for mass transfer to be evaluated and hence, its impact on the volumetric mass transfer coefficient can be assessed. The additional novelty of the online method developed in this study is that the classical unit-cell model used to describe the mass transfer process has been modified in order to take into account the drastic changes of fluid properties and related volume changes of the phases that occur at high pressure.

The following sections describe the experimental setup, the colorimetric technique, the revised unit-cell model, as well as the calculation of dissolved CO_2 concentration and mass transfer coefficients. The described method is then used for the determination of $k_L a_L$, k_L and a_L in a two-phase flow of H_2O and CO_2 at 10 MPa and 303 K at various flow rates. For the sake of simplicity, in the remainder of this paper the CO_2-rich phase is referred to "fluid phase" and the H_2O-rich phase is referred to the "liquid phase".

2. Experimental setup

The experimental setup consists in the integration of an in-house microreactor in an environment that allows the fluids to be fed at high pressure in order to obtain a stable two-phase segmented flow. The microreactor is composed of fused silica capillaries embedded in epoxy resin to improve pressure resistance; this method was adapted from Macedo Portela da Silva et al. (2014). The inner diameter of the main capillary is 250 μm and the capillary is 38.2 cm long. CO_2 and H_2O are fed co-currently inside the microreactor. CO_2 is injected in the main capillary using a coaxial capillary tube with a smaller diameter (100 μm OD, 80 μm ID). The entire setup guarantees constant temperature and pressure, and it allows image acquisition of the flow through an optical window. A schematic diagram of the complete setup is shown in Fig. 1:

Water and carbon dioxide are fed to the microreactor at constant pressure using two high-pressure syringe pumps. An ISCO 260 D pump (Teledyne ISCO) is used for H_2O injection and an ISCO 100 HLX pump is used for CO_2 injection. A Coriolis-effect mass micro-flowmeter (Bronkhorst) is placed between the CO_2 injection pump and the microreactor in order to measure the mass flow rate of CO_2 at the inlet. The connections between the pumps and the microreactor are made using stainless steel tubes with an internal diameter of 0.6 mm. The fluids are distributed using pressure-resistant valves. The stainless-steel tubes are connected to the bulkheads of the temperature-controlled chamber and the bulkheads are connected to the microreactor placed within the chamber. A third pump (ISCO 260 D) is connected to the outlet of the microreactor in order to collect the two-phase mixture and to maintain constant pressure within the microreactor. The three syringe pumps can operate with constant volumetric flow rate or constant pressure. In this experimental campaign, the feeding pumps for H_2O and CO_2 are operated with a fixed volumetric flow rate, while the outlet pump is operated at constant pressure. Check valves are present between the fluid injection pumps and the microreactor in order to prevent back flow of H_2O (or CO_2) into the CO_2 pump (or H_2O pump) during the generation of a stable periodic gas-liquid flow. In addition, filters (with an average pore diameter of 0.5 μm) are inserted at the same places as the valves in order to prevent the contamination of the microreactor with possible impurities from the injection pumps.

The precision of the pressure maintained by the outlet pump (ISCO 260 D) given by the manufacturer is ±0.26 MPa, which corresponds to 0.5% of the full scale (51.7 MPa). The maximum pressure drop in the system has been calculated for the worst-case scenario, i.e. when the outer capillary tube of the microreactor and the stainless-steel tubes are filled with water and when the total flow rate in the system is at the maximum value used in the experimental campaign (350 μL min^{-1}). For this case, the maximum possible pressure drop does not exceed 350 hPa, therefore pressure drop is considered negligible in this study and no impact of pressure drop on fluid properties is expected.

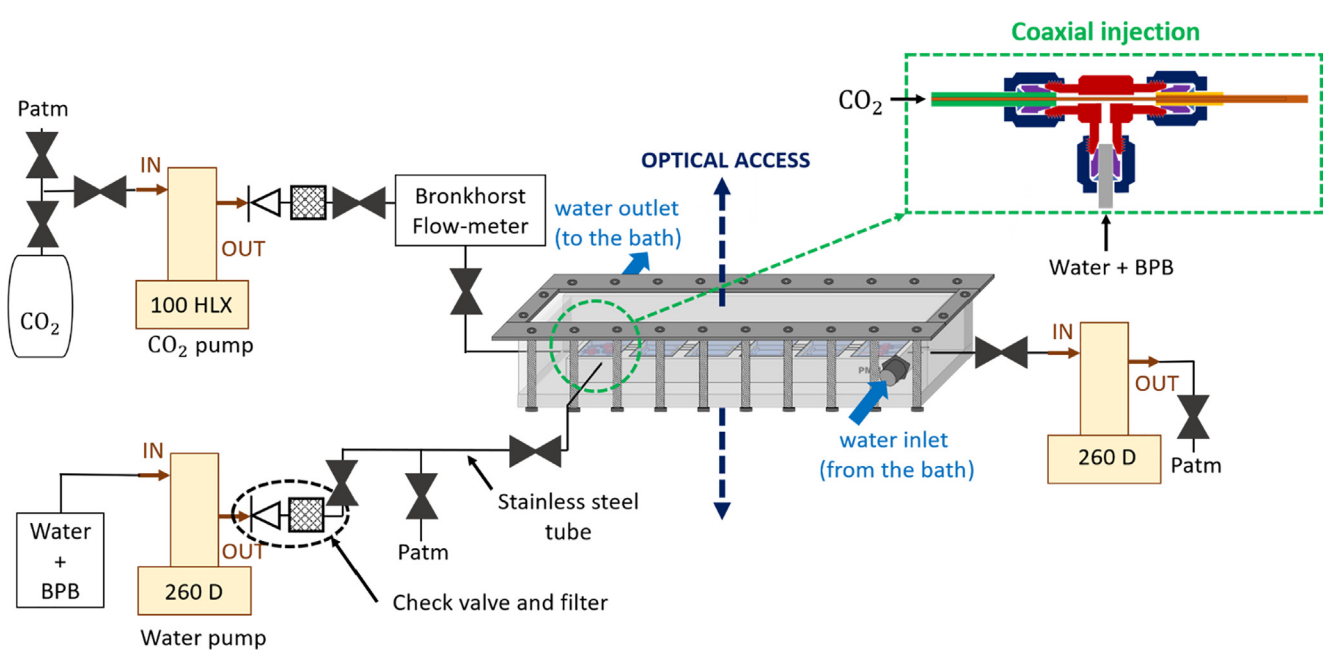

Fig. 1. Schematic diagram of the experimental setup used to determine mass transfer coefficients in high-pressure two-phase flows.

The temperature for the experimental setup is controlled at two strategic locations. Firstly, the microreactor is placed in a temperature-controlled chamber, as shown in Fig. 1. This chamber is connected to a thermostatically controlled bath (Lauda RE 2025G) using heat-insulated plastic tubes. The temperature in the bath is regulated at ±0.01 K. Heat losses along the insulated tubes give an uncertainty on the water temperature of ±0.1 K. The CO_2 syringe pump is also temperature controlled. A jacket connected to an external bath (Lauda RE 104) surrounds the pump in order to maintain the CO_2 in a liquid state (282 K).

2.1. Operating conditions

The operating conditions for pressure and temperature are 10 MPa and 303 K, respectively. As previously mentioned, the inlet ISCO pumps are set to deliver a constant volumetric flow rate. However, since there is a temperature change – and therefore a density change of CO_2 – between the pumps and the microreactor inlet, the volumetric flow rates have to be recalculated to take into account the change in density. Hence, the volumetric flow rates given in this paper are calculated at 303 K and 10 MPa. The ranges of flow rates used during the experimental campaign are $\dot{V}_{H_2O}$ =110–350 μLmin^{-1} ($Re_L = \frac{\rho_L U_L D}{\mu_L} = 11.7 - 37.2$) and $\dot{V}_{CO_2}$ =59–112 μLmin^{-1} ($Re_F = \frac{\rho_F U_F D}{\mu_F} = 49.5 - 94$). Further details on the operating conditions are given in Appendix A.

2.2. Camera setup

The microreactor is illuminated by transmitted light using a lighting system consisting of four LEDs (CXB3590 3000 K 80 CRI). The images of the flow inside the microreactor are obtained using a high-speed camera (Baumer HXC13, 2000 fps, 1280 × 1040 pixels^2) with a band pass filter (590 nm ± 2 nm), which is placed directly above the LED system and the microreactor. Images covering 1.8 mm of capillary length were taken at 600 fps. The microreactor has four viewing windows, each comprising four measurement spots where the capillary (stripped of its protective coating) is visible. The device is shown schematically in Fig. 2. The camera-LED assembly is placed on a mobile rail in order to focus on the different measurement spots whilst maintaining the same lighting quality for each image.

Four high-intensity LEDs (CXB3590 3000 K 80 CRI, 10,000 lm each) are arranged to provide a strong signal since the pass band filter greatly reduces light intensity. These four LEDs are positioned in a concave manner to achieve maximum illumination in the capillary tube. In addition, these LEDs deliver maximum intensity at the wavelength of the band pass filter (590 nm). Each of the LEDs are placed on a static fan, which is placed on a dynamic fan in order to dissipate the heat produced by the LEDs. Two rectangular reflectors are located on either side of the lighting system and parallel to the capillary. These reflectors allow to better define the contours of the capillary and the bubbles. A macro-extension tube with a 2x teleconverter is set to the high-speed camera for macro photography. The distance between the camera lens and the capillary is 120 mm. The field of view of the camera is a rectangle of 1.8 mm length, which corresponds to an image resolution of 6.8 μm per pixel. The distance between the object inside the capillary and the lighting system is adjusted to obtain uniform illumination over the entire viewing field of the camera. The iris opening is adjusted to f/2.4 (where f is the focal length) in order to decrease the depth of focus and obtain a clear image in the capillary plane only. The camera shutter is set at 300 μs, which is short enough to avoid motion blur due to the speed of the slugs in the flow.

3. High-pressure unit-cell model

In a two-phase segmented flow of water and carbon dioxide, a unit cell is composed of one CO_2 segment considered here as a bubble, one H_2O-rich liquid segment, considered here as a slug, and a liquid film surrounding the bubble and the slug. At low capillary numbers, the liquid film thickness can be approximated by the correlation proposed by Bretherton (1961)

$\frac{\delta}{R} = 1.34 {Ca_B}^{2/3}$ where R is the CO_2 bubble radius, δ is the liquid film thickness and $Ca_B = U_B \mu_F / \sigma$. In this work where $Ca_B < 10^{-3}$, the correlation estimates the liquid film thickness to be less than 1.3 % of the capillary tube radius, i.e. less than 2 μm thick. Therefore, the liquid film can be considered as negligible and the unit-cell model of the two-phase flow can be depicted as in Fig. 3. In this model, a unit-cell is composed of one CO_2 segment with volume V_b delimited by the surface S_b, and one H_2O-rich liquid segment of volume V_L, which is delimited by its surface S_L composed of S_{cap}, S_{in}, S_{out} and S_b.

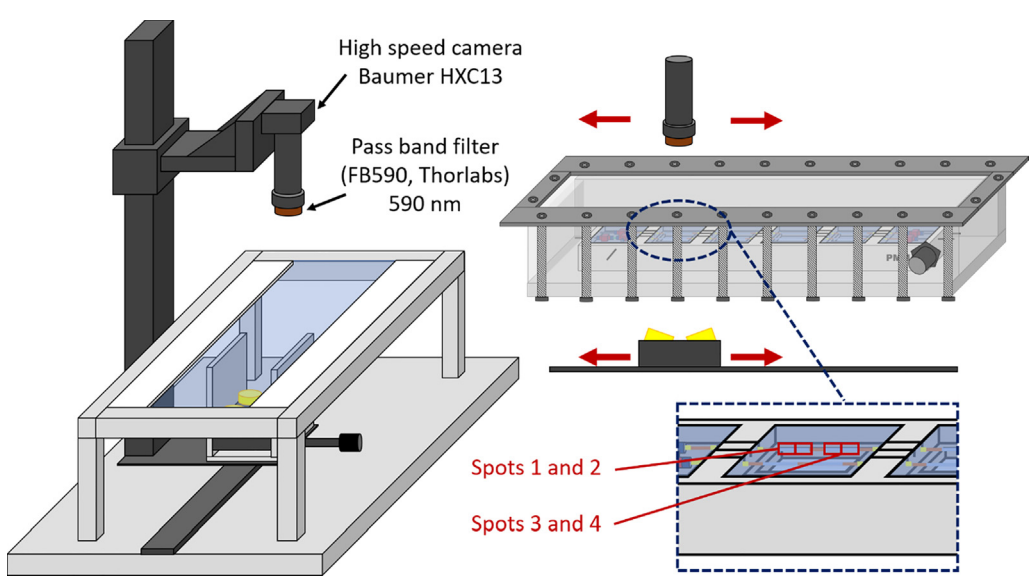

Fig. 2. Schematic overview of the optical measurement setup. A translating system makes it possible to acquire images at the different measurement spots.

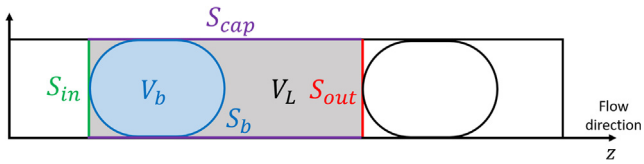

Fig. 3. Presentation of the unit-cell model, which is composed of one CO_2 segment with volume V_b delimited by the surface S_b, and one H_2O-rich liquid segment of volume V_L, which is delimited by its surface S_L composed of S_{cap}, S_{in}, S_{out} and S_b.

Fig. 4 presents the direction of the molar flux $N^b_{CO_2}$ at the interface between the bubble and the liquid slug due to convection and diffusion, as well as the combined molar flux between two consecutive unit-cells ($N^{in}_{CO_2}$ and $N^{out}_{CO_2}$). The volumetric mass transfer coefficient $k_La_L(z)$ can then be determined by integrating the partial mass balance of CO_2 over a finite volume of the H_2O-rich slug, The result is presented in Equation (1) and the demonstration is shown in detail in Appendix B:

$$k_La_L(z) = \frac{U_{TP}}{C^*_{CO_2}(T,P) - \langle C_{CO_2}\rangle(z)} \cdot \frac{d\langle C_{CO_2}\rangle}{dz} \tag{1}$$

In this equation, $k_La_L(z)$ is a function of the two-phase velocity $U_{TP} = \left(\dot{V}_{H_2O} + \dot{V}_{CO_2}\right)/S$, the average concentration of CO_2 in the liquid slug $\langle C_{CO_2}\rangle(z)$, the first derivative of this concentration $\frac{d\langle C_{CO_2}\rangle}{dz}$ and the equilibrium concentration of CO_2 in the liquid slug $C^*_{CO_2}(T,P)$, where z is the axis location inside the microreactor ($z = 0$ corresponds to the point where CO_2 and H_2O are contacted). The volumetric mass transfer coefficient k_La_L is hence computed at different axial positions along the capillary tube and to do this, $\langle C_{CO_2}\rangle$ and $\frac{d\langle C_{CO_2}\rangle}{dz}$ are determined at each position using the colorimetric method.

It should be pointed out, however, that Equation (1) may not be valid in some situations, as follows:

- If the density of the liquid mixture varies along the capillary tube due to the dissolution of CO_2 in the liquid phase, which modifies the convective term of the total flux.
- If the length of the liquid slug in the segmented flow is significantly greater than the length of the gas bubble (at least one order of magnitude higher).
- If the solute from the liquid phase is soluble within the gas phase (therefore global and local coefficients are different and $K_L \neq k_L$).
- If the caps of the bubble are not hemispherical.
- If the liquid film thickness is non-negligible.

Is this study, the above-mentioned situations do not occur.

4. Colorimetric method

The colorimentric method used in this work to determine mass transfer is based on the change in colour of a pH indicator due to the dissolution of CO_2 in water.

4.1. Bromophenol blue

Bromophenol blue (BPB) is a pH sensitive indicator and is employed here to follow the acidification of water by CO_2. The absorbance of BPB is a function of the pH of the aqueous solution, as shown in Fig. 5, which presents the visible absorbance spectra of BPB solutions at different values of pH.

The absorption spectrum of BPB shows an acidic form with a maximum absorbance at 410 nm and a basic form with a maximum absorbance at 590 nm. These absorbance maxima are a function of the pH of the solution. An aqueous solution of BPB that observed in the capillary tube, therefore exhibits a variation in absorbance and color, which are depicted by a variation in greyscale, if the pH changes. In a two-phase flow of carbon dioxide and water mixed with BPB, the acidification of water due to the dissolution and transfer of carbon dioxide is detected by means of a change in greyscale. This change in greyscale is detectable since the camera filter only allows light of a wavelength equal to the maximum absorbance peak of the basic form of BPB to pass through.

4.2. Calibration curve

The variation in greyscale is correlated with a variation of pH using a calibration curve, which is determined with BPB buffer solutions. Ten buffer solutions composed of citric acid, sodium citrate and BPB are prepared for pH values ranging from 1.88 to 6.23, for a concentration [BPB] = 0.8 mmol·L^{-1}. These solutions are injected inside the microreactor and the greyscale values are

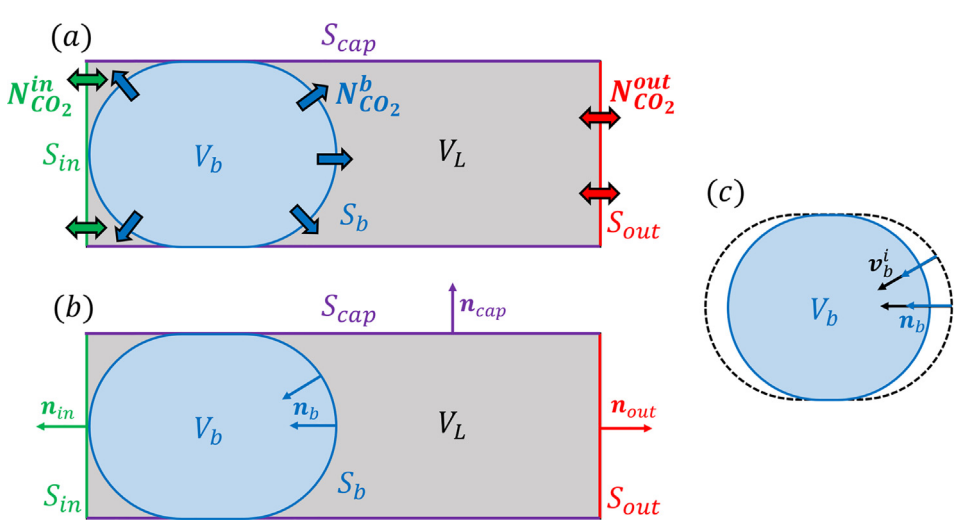

Fig. 4. (a) Unit-cell and combined molar flux of CO_2 transferring through the H_2O-rich liquid slug surface. (b) Unit-cell and normal vectors of each H_2O-rich liquid slug surfaces. (c) CO_2-rich bubble shrinkage where $\boldsymbol{v}^i_b$ is the bubble interface velocity vector.

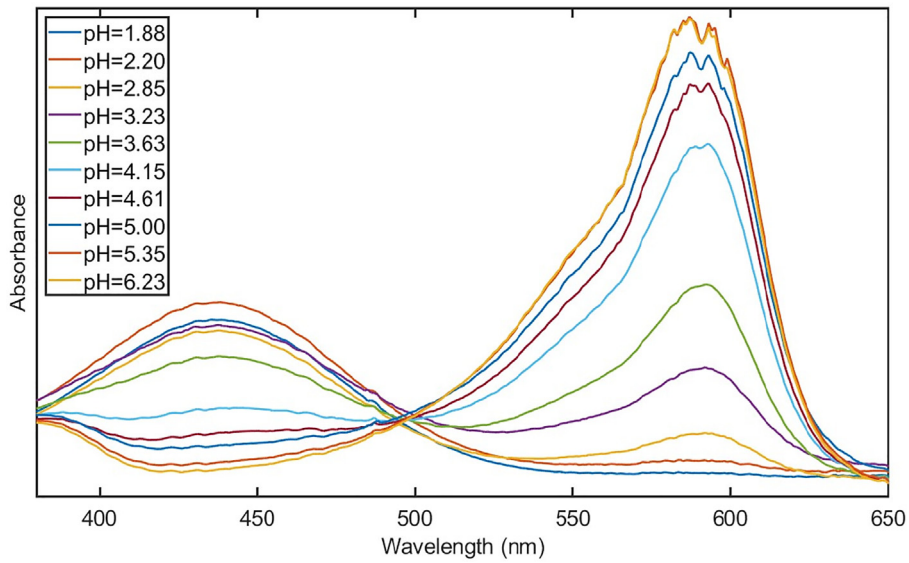

Fig. 5. Visible absorbance spectra (Agilent Technologies Cary 8454) of pH buffer aqueous solutions (citric acid + sodium tri-citrate) with a bromophenol blue concentration equals to 0.03 mmol·L^{-1}. (For interpretation of the references to color in this figure legend, the reader is referred to the web version of this article.)

extracted from camera images. A blank image has been removed from each of the images of the BPB solutions in order to take into account the differences in color intensity across the radius of the tube due to the variation of depth of fluid. The calibration curve is shown in Fig. 6. A logistic regression is used to fit the experimental points. It can be observed that for pH values higher than 5, the error on pH increases. However, in this study, the H_2O-rich phase is acidified by CO_2 directly at the bubble generation process, and therefore pH values that are greater than 5 are not encountered.

4.3. Image analysis

1800 images of the two-phase flow are taken for each set of experimental conditions and at each of the 10 measurement spots (from the contacting zone up to an axial position z = 19 cm). The images are processed using a Matlab code that allows bubble and slug velocities, lengths, surface areas and volumes, as well as the greyscale value in the liquid slugs to be obtained. Fig. 7 presents an example of the evolution of the greyscale value of the water-rich phase at the center of the capillary as a function of the position along the z-axis of the capillary tube. A total of 1.8 billion of greyscale values are analysed for each experiment and a simple exponential-type model is fitted for each data set that provides a relationship between greyscale and the axial position along the capillary tube, z. Fig. 8 presents various greyscale profiles obtained with this method.

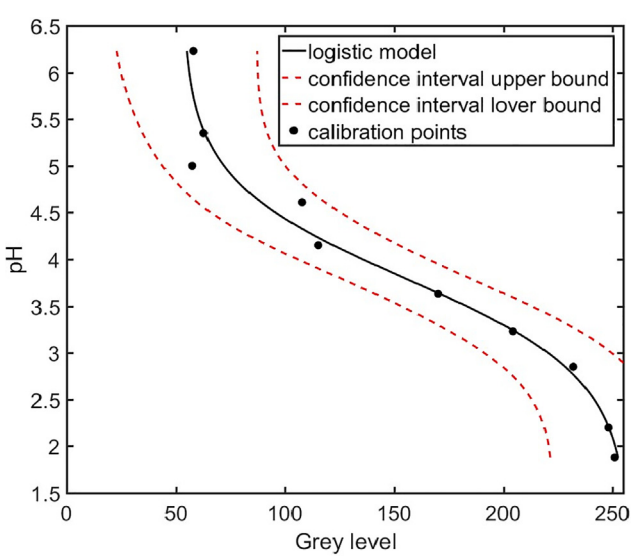

Fig. 6. Calibration curve linking the pH of the buffer solutions (citric acid + sodium tri-citrate) with the greyscale of the images of these solutions placed inside the microreactor. [BPB] = 0.8 mmol·L^{-1}, shutter opening time = 300 μs.

4.4. Determination of pH

The greyscale values along the microreactor are converted to pH values using the calibration curve presented previously. Example results are presented in Fig. 9. It can be observed that the pH decreases exponentially along the channel as CO_2 is transferred from the bubble to the water-rich liquid slug. The pH tends to a constant value when thermodynamic equilibrium is reached. In addition, as the volumetric flow rate ratio $\dot{V}_{CO_2}/\dot{V}_{H_2O}$ increases, thermodynamique equilibrium is reached closer to the gas-liquid generation zone. Uncertainty calculations are presented in Appendix C.

4.5. Determination of C_{CO_2}

When carbon dioxide is dissolved in an aqueous solution, it is present under different forms: CO_2,carbonic acid H_2CO_3, bicarbonate ions HCO_3^- and carbonate ions CO_3^{2-}. Hence, different chemical equilibria occur simultaneously. A speciation model can enable the concentration of CO_2 dissolved in water to be determined from the concentration of H^+, which is obtained from pH values. However, the speciation model commonly employed in the litterature (see Toews et al., 1995 for example) overestimates the concentration of CO_2 dissolved at high-pressure. Since the model is not well adapted for high-pressure studies, the experimental data obtained at temperatures between 308 K and 423 K for pressures up to 15 MPa in the work of Peng et al. (2013) are used in this work to correlate the measured pH values with the CO_2 concentration in the H_2O-rich phase.

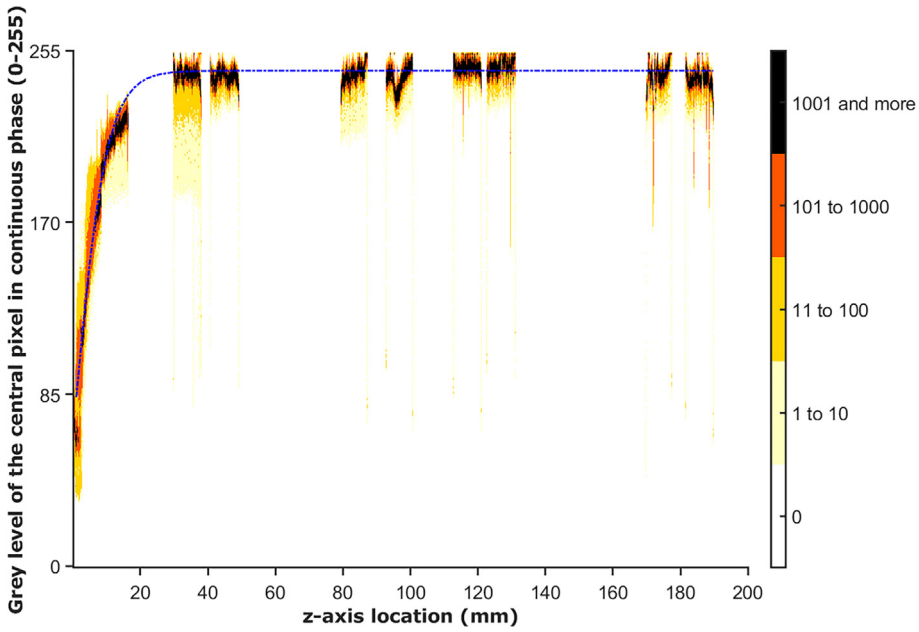

Fig. 7. Greyscale at the center of the capillary inside the liquid slugs along the entire microreactor. The operating conditions are P = 10 MPa, T = 303 K, $\dot{V}_{CO_2}$ = 58.9 μL·min^{-1}, $\dot{V}_{H_2O}$= 150 μL·min^{-1}. The color scale represents the number of greyscale values out of all 1800 values obtained at the specific axial position. The dashed line corresponds to an exponential type model for the greyscale value along the microreactor that is weighted by the number of points (color level).

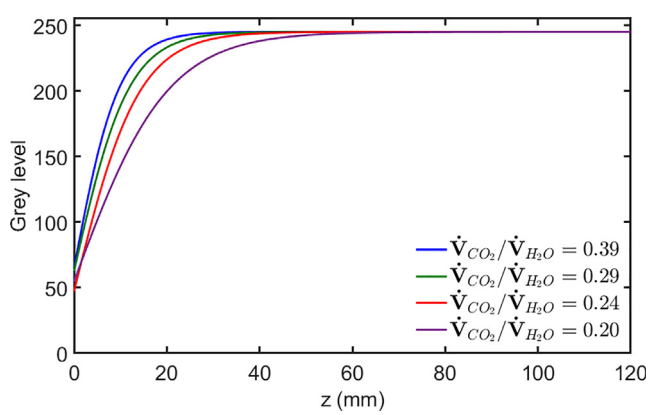

Fig. 8. Greyscale profiles (0–255) obtained in the H_2O-rich slugs versus the z-axis position at 10 MPa and 303 K where $\dot{V}_{CO_2}$ = 58.9 μL·min^{-1} at various $\dot{V}_{H_2O}$ flowrates.

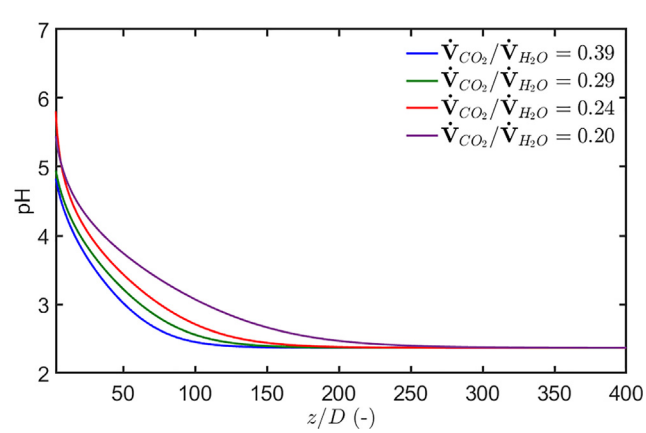

Fig. 9. pH profiles obtained in the H_2O-rich slugs versus the dimensionless position along the axis at 10 MPa and 303 K where $\dot{V}_{CO_2}$ = 58.9 μL·min^{-1} at various $\dot{V}_{H_2O}$ flowrates.

4.6. Determination of k_La_L

The CO_2 concentrations obtained in this work correspond to discrete values due to the use of experimental data from Peng et al. (2013). In order to obtain concentration curves, which are required to calculate the first derivative of the concentration for the determination of the volumetric mass transfer coefficient, the CO_2 concentration values along the microchannel are filtered with a fast Fourier transform (FFT) algorithm as presented in our previous work (Deleau et al., 2020). The normalized concentration profiles obtained with the FFT algorithm are then used to compute the first derivative of CO_2 concentrations, $\frac{dC_{CO_2}}{dz}$. Using the values of C_{CO_2} and $\frac{dC_{CO_2}}{dz}$ at various z axis-locations, the volumetric mass transfer coefficient k_La_L is then finally determined using Equation (1).

5. Results and discussion

This section presents the CO_2concentration profiles and the volumetric mass transfer coefficient k_La_L along the capillary tube obtained with the colorimetric method. The impact of CO_2 and H_2O flow rates on the transport process at 10 MPa and 303 K is explored. Prior to this, the characteristics of CO_2-H_2O two-phase segmented flow (i.e. bubble and liquid slug lengths, specific liquid surface area and bubble velocity) are analysed since these are necessary for understanding the transport phenomena.

5.1. Characteristics of CO_2-H_2O two-phase segmented flow

Figs. 10–12 present photos of the generation of CO_2 bubbles in H_2O with BPB indicator at 10 MPa and 303 K. As the CO_2 bubbles move along the capillary tube from left to right, CO_2 dissolves into the water-rich slug and the BPB indicator changes colour due to the decrease in pH. This is depicted by the change in greyscale, from black to light grey in the direction of the flow.

The characteristics of the segmented flows in Figs. 10–12 are analysed to determine the bubble velocity (U_B), the bubble length (L_B) and the liquid slug length (L_S) as a function of volumetric flow

Fig. 10. Generation of a two-phase segmented flow of CO_2 and BPB/H_2O for 10 MPa and 303 K where $\dot{V}_{CO_2}$ = 58.9 μL·min^{-1}: (a) $\dot{V}_{H_2O}$ = 150 μL·min^{-1}, (b) $\dot{V}_{H_2O}$ = 200 μL·min^{-1} and (c) $\dot{V}_{H_2O}$ = 300 μL·min^{-1} .

Fig. 11. Generation of a two-phase segmented flow of CO_2 and BPB/H_2O for 10 MPa and 303 K where $\dot{V}_{H_2O}$ = 350 μL·min^{-1}: (a) $\dot{V}_{CO_2}$ = 76.6 μL·min^{-1}, (b) $\dot{V}_{CO_2}$ = 94.2 μL·min^{-1} and (c) $\dot{V}_{CO_2}$ = 111.9 μL·min^{-1} .

Fig. 12. Generation of a two-phase segmented flow of CO_2 and BPB/H_2O for 10 MPa and 303 K where $\dot{V}_{CO_2}$ = 82.5 μL·min^{-1}: (a) $\dot{V}_{H_2O}$ = 110 μL·min^{-1}, (b) $\dot{V}_{H_2O}$ = 150 μL·min^{-1}, (c) $\dot{V}_{H_2O}$ = 200 μL·min^{-1} and (d) $\dot{V}_{H_2O}$ = 300 μL·min^{-1}.

rate ratio $\dot{V}_{CO_2}/\dot{V}_{H_2O}$. In addition, the specific surface area, a_L, defined by the bubble surface area divided by the volume of liquid slug of the same unit-cell, is calculated. The image analysis method presented previously allows around 18,000 values of each of the parameters (speed, lengths and specific area) to be obtained for each measurement spot.

Fig. 13 presents the bubble velocity, U_B, as a function of the two-phase flow velocity U_{TP}. The bubble velocity increases linearly with the velocity of the two-phase flow and is slightly greater than the velocity of the two-phase flow. Indeed, following a simple mass balance across a unit cell it can be shown that $U_B = U_{TP}$, when there is no liquid film. Here, $U_B = 1.1U_{TP}$, which confirms that a very

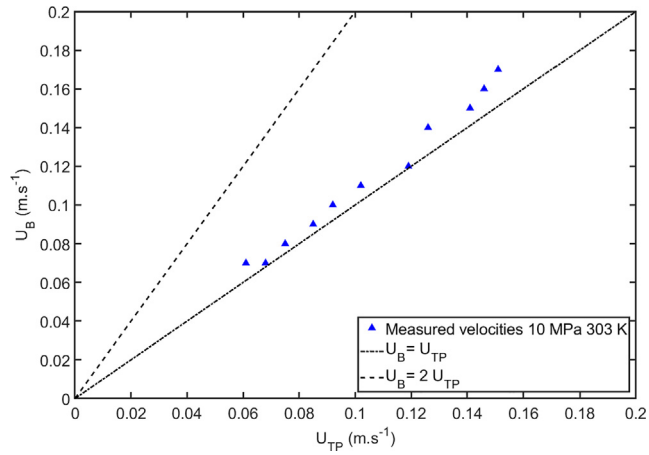

Fig. 13. Bubble velocity U_B as a function of the two-phase velocity $U_{TP} = (\dot{V}_{H_2O} + \dot{V}_{CO_2})/S$ for all experiments at 10 MPa and 303 K.

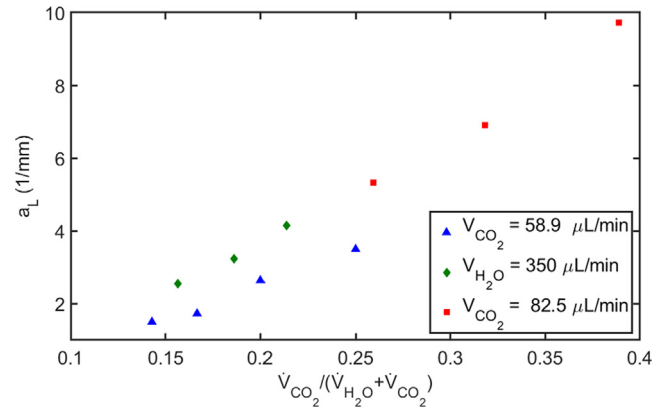

Fig. 16. Specific surface area a_L at z = 2.95 cm at 10 MPa and 303 K versus $\dot{V}_{CO_2}/(\dot{V}_{CO_2} + \dot{V}_{H_2O})$. Note that $\dot{V}_{CO_2}/(\dot{V}_{CO_2} + \dot{V}_{H_2O})$ increases with $\dot{V}_{CO_2}/\dot{V}_{H_2O}$.

thin liquid film is present around the bubbles, as predicted by Bretherton's correlation, and that the liquid film can be considered as negligible in this work. The limit $U_B = 2U_{TP}$ corresponds to "free" bubbles flowing at the center of the capillary with a Poiseuille velocity profile.

Figs. 14–16 show the influence of the volumetric flow rates $\dot{V}_{CO_2}, \dot{V}_{H_2O}$ on the bubble length L_B, the slug length L_S and the specific surface area a_L measured z = 2.95 cm. Firstly, it is observed that when the volumetric flow rate ratio $\dot{V}_{CO_2}/\dot{V}_{H_2O}$ increases, the bubble length L_B and the specific surface a_L increase, whilst the liquid slug length L_S decreases. It can be seen in Fig. 14 that the bubble length L_B is linearly dependent on the volumetric flow rate ratio $\dot{V}_{CO_2}/\dot{V}_{H_2O}$; this is in agreement with the well-known Garstecki model for bubble and drop generation in T-junctions (Garstecki et al., 2006; van Steijn et al., 2007). Fig. 15 shows that the liquid slug length L_S, increases linearly with $\dot{V}_{H_2O}/\dot{V}_{CO_2}$, which corresponds to the slug formation described by (Völkel, 2009). Fig. 16 shows that the specific surface area a_L increases linearly with $\dot{V}_{CO_2}/(\dot{V}_{CO_2} + \dot{V}_{H_2O})$. This is due to the fact that $\frac{L_S}{D} \sim 1 + \delta \frac{\dot{V}_{H_2O}}{\dot{V}_{CO_2}}$ with δ a constant and $a_L \sim \frac{D^2}{DL_S} = \frac{D}{L_S}$).

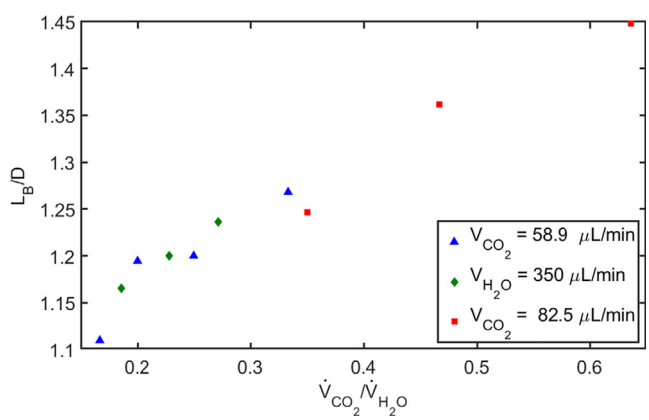

Fig. 14. Normalized bubble length L_B at z = 2.95 cm at 10 MPa and 303 K versus of the volumetric flow rate ratio $\dot{V}_{CO_2}/\dot{V}_{H_2O}$.

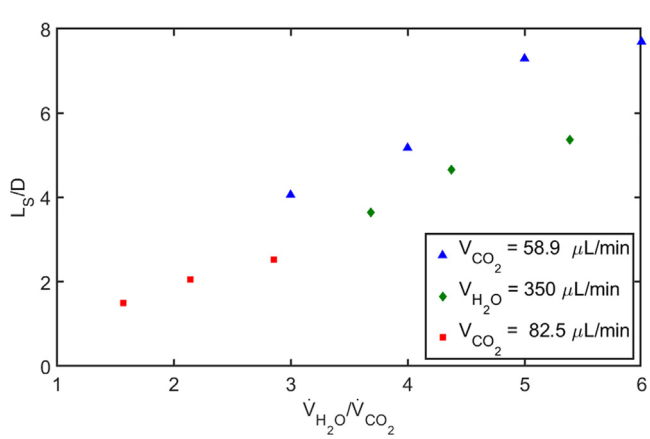

Fig. 15. Normalized slug length L_S at z = 2.95 cm at 10 MPa and 303 K versus the volumetric flow rate ratio $\dot{V}_{H_2O}/\dot{V}_{CO_2}$.

5.2. CO_2 concentration profiles

Fig. 17 (a, b, c) shows the impact of the gas-to-liquid flow rate ratio on the the normalized concentration profiles for different constant gas or liquid flow rates along the capillary tube. It is observed in Fig. 17 (a, b) that when the volumetric flow rate ratio $\dot{V}_{CO_2}/\dot{V}_{H_2O}$ increases with a constant CO_2 flow rate, thermodynamic equilibrium is reached closer to the bubble generation zone (z/D = 0), i.e. in a shorter distance along the tube. This can be explained by the physical characteristics of the two-phase flow. Indeed, as shown in Fig. 14 and Fig. 16, when the ratio $\dot{V}_{CO_2}/\dot{V}_{H_2O}$ increases, both the bubble length L_B and the specific surface area a_L increase, thereby increasing area for mass transfer. In addition, the liquid slug length L_S decreases when $\dot{V}_{CO_2}/\dot{V}_{H_2O}$ increases and therefore, the amount of water to be saturated (i.e. the liquid slug volume) is smaller. As a result, the mass transfer rate increases and the liquid slugs are saturated more quickly, and hence thermodynamic equilibrium is reached in a shorter length (and time). The same effect is observed in Fig. 17 (c) where the volumetric flow rate of water is constant, however, since the two-phase velocity U_{TP} varies very little ($\dot{V}_{H_2O} \gg \dot{V}_{CO_2}$) in these experiments, the residence time as well as the location where the thermodynamic equilibrium is reached hardly change.

5.3. Volumetric mass transfer coefficient profiles

Fig. 18 (a, b, c) show the evolution of the volumetric liquid mass transfer coefficient $k_L a_L$, determined with Equation (1), along the

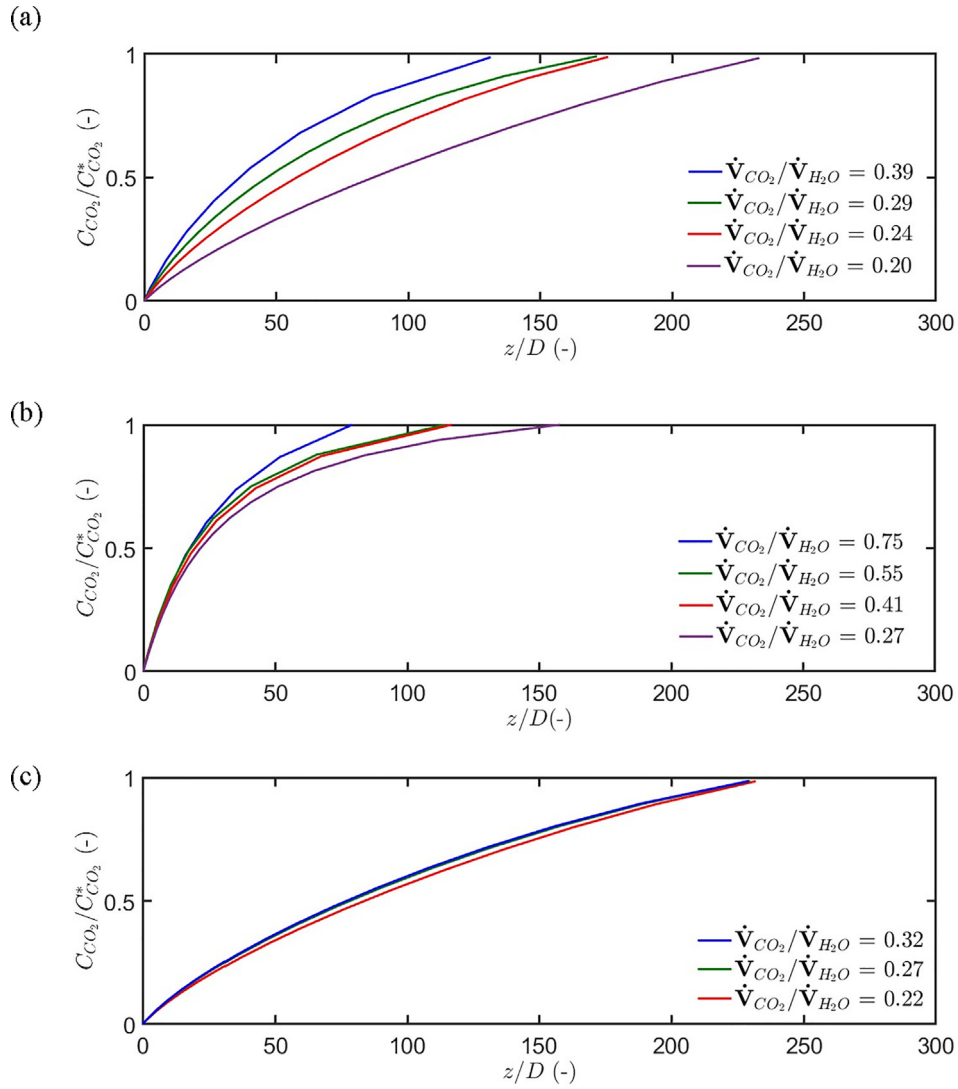

Fig. 17. (a) Normalized fitted concentration profiles of CO_2 in the H_2O-rich phase versus the normalized position along the length of the capillary tube at 10 MPa and 303 K at $\dot{V}_{CO_2}$ = 58.9 μL·min^{-1}. (b) $\dot{V}_{CO_2}$ = 82.5 μL·min^{-1}. (c) $\dot{V}_{H_2O}$ = 350 μL·min^{-1}.

capillary tube for different volumetric flow rate ratios. Firstly, it can be seen that k_La_L is not constant along the microreactor; depending on the operating conditions, the volumetric mass transfer coefficient is 5–15 times higher close to the bubble generation zone compared with at the end of the tube. This is similar to what was found by (Deleau et al., 2020; Tan et al., 2012; Abolhasani et al., 2015) for various gas-liquid systems at both high and ambient pressure. Using the measured values of a_L obtained via image analysis, it is possible to deduce the value of k_L at different positions along the capillary tube to better understand why k_La_L is higher in the bubble generation zone. Table 1 presents values of k_La_L, k_L and a_L at two positions (z/D = 6 and z/D = 100) along the tube. It can be observed that the k_La_L values decrease between z/D = 6 and z/D = 100. Indeed, from this data, it can be seen that both a_L and k_L decrease between these two axial locations. However, on average, a_L is about 40% higher close to the bubble generation zone compared with at the end of the capillary, whilst k_L is 125% greater. This significantly higher value of k_L close to the bubble generation zone may be explained by the transient nature of the bubble formation process and the associated changes in local velocity gradients, compared with the more stable, pseudo-stationary flow occurring further along the capillary tube (z/D = 100). This may also be explained by the increased effectiveness of the liquid film in the bubble generation zone for mass transfer compared with that in developed Taylor flow further along the capillary tube. Indeed, during the bubble formation process, the velocity gradients in the liquid film surrounding the bubble are continually changing (Van Steijn et al., 2007), which may result in the enhancement of the liquid phase mass transfer coefficient k_L. The combination of both higher a_L and k_L close to the bubble generation zone explains why 20–40% of the total mass transfer process occurs in this zone under the operating conditions investigated in this paper. This observation agrees with the study by Tan et al. (2012) where the duration of the bubble generation process is of the same order of magnitude. Indeed, if the bubble generation process is faster, the enhancement of mass transfer at the contacting zone can be reduced to 2–10% compared with at the end of the channel (Abolhasani et al., 2015). Mass transfer in the bubble generation zone also highly depends on the duration of the generation process and the inlet geometry. Indeed, mass transfer during the bubble generation process can also be lower or almost equal to the mass transfer occurring in developed Taylor flow further in the

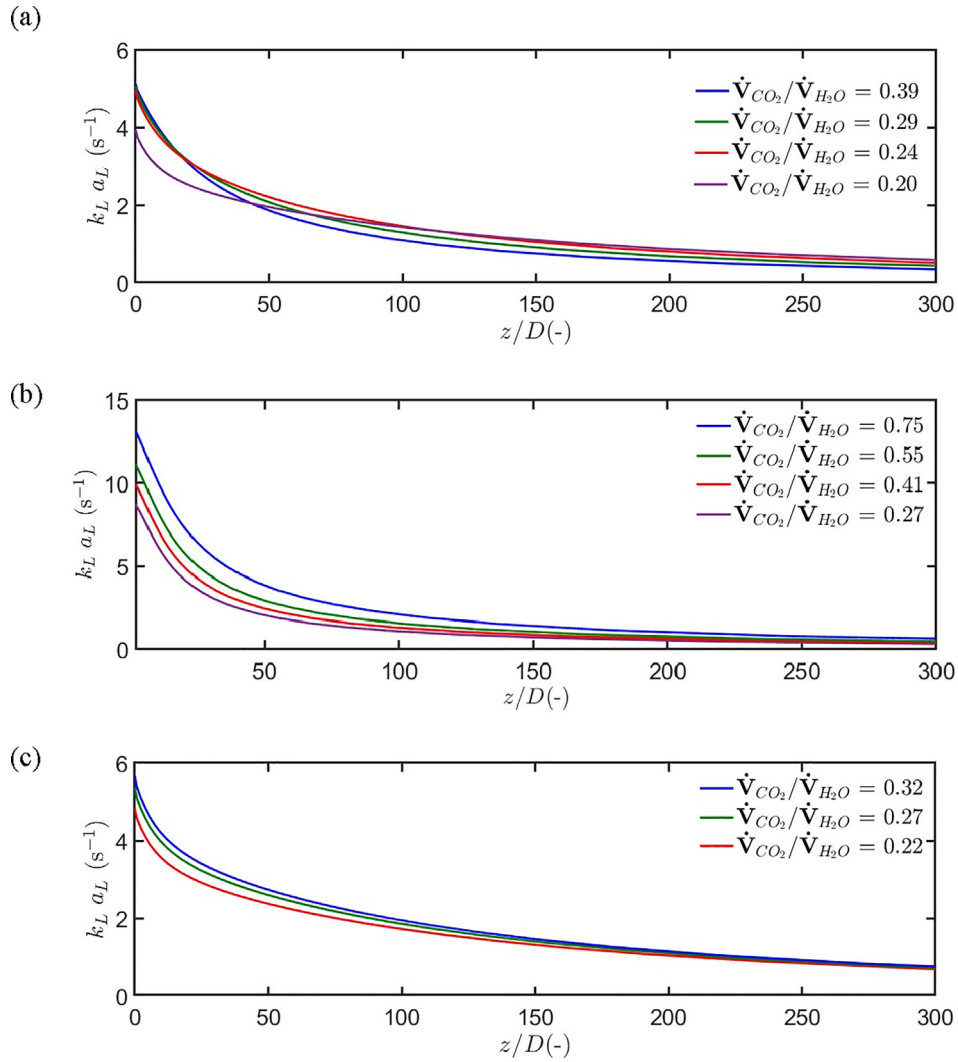

Fig. 18. Volumetric liquid mass transfer coefficient profiles versus the normalized z-axis location at 10 MPa and 303 K at (a) $\dot{V}_{CO_2}$ = 58.9 μL·min^{-1}. (b) $\dot{V}_{CO_2}$ = 82.5 μL·min^{-1}. (c) $\dot{V}_{H_2O}$ = 350 μL·min^{-1}.

Table 1
Decoupling of the specific surface a_L and the local mass transfer coefficient k_L effects on the volumetric mass transfer coefficient k_La_L.

	k_La_L (s^{-1})		a_L (mm^{-1})		k_L (mm · s^{-1})	
$\frac{\dot{V}_{CO_2}}{\dot{V}_{H_2O}}$	z/D = 6	z/D = 100	z/D = 6	z/D = 100	z/D = 6	z/D = 100
$\dot{V}_{CO_2} = 58.9\ \mu L \cdot min^{-1}$						
0.39	5.12	1.25	4.80	3.90	1.07	0.32
0.24	4.95	1.51	2.80	1.92	1.77	0.79
0.2	3.93	1.58	2.25	1.49	1.75	1.06
$\dot{V}_{H_2O} = 350\ \mu L \cdot min^{-1}$						
0.32	5.67	1.95	5.50	4.26	1.03	0.46
0.27	5.37	1.88	4.70	3.41	1.14	0.55
0.22	4.82	1.77	3.67	2.55	1.31	0.69

microchannel depending on these parameters (Liu et al., 2021; Zhao et al., 2021)

The impact of the volumetric flow rate ratio on mass transfer is also observed from Fig. 18. The graphs show that for constant $\dot{V}_{CO_2}$ or $\dot{V}_{H_2O}$, an increase in $\dot{V}_{CO_2}/\dot{V}_{H_2O}$ leads to an increase in k_La_L. This is in agreement with the results obtained by Deleau et al. (2020). As shown in Fig. 16, an increase in $\dot{V}_{CO_2}/\dot{V}_{H_2O}$ results in an increase in a_L (so there is more interfacial area available for mass transfer). It can be seen in Table 1 that an increase in $\dot{V}_{CO_2}/\dot{V}_{H_2O}$results in a decrease in k_L. Therefore, the increase in k_La_L with $\dot{V}_{CO_2}/\dot{V}_{H_2O}$(for constant $\dot{V}_{CO_2}$ or $\dot{V}_{H_2O}$) is driven by the increase in specific surface a_L.

The values of the volumetric mass transfer coefficients measured here for a CO_2-H_2O system are between 1 s^{-1} and 13 s^{-1}. This

order of magnitude is similar to that obtained for the same system using the Raman spectroscopy method (0.2 s^{-1} to 4 s^{-1}) described by Deleau et al. (2020). This difference between the results is, at least in part, due to the slightly larger capillary diameter (300 μm) employed in Deleau et al. (2020) compared with 250 μm capillary tube diameter used in this study. Indeed, the mass transfer characteristic time, which is proportional to the square of the diameter, is 1.4 times higher with a diameter of 250 μm compared with that obtained in a capillary tub with a diameter of 300 μm.

6. Conclusion

In this study, a method was developed to determine the liquid volumetric mass transfer coefficient in a two-phase segmented flow at high pressure in a microcapillary tube. This method is based on the use of a colorimetric indicator and involves high-speed image acquisition, image processing, statistical analyses, pH calibration, FFT, a thermodynamical model for two-phase mixtures and the revised unit-cell model. Since the method is mainly based on flow visualization, it also allows the physical characteristics of the two-phase flow (i.e. bubble, slug and unit-cell lengths, bubble velocity and specific surface area) to be determined along the microchannel length simultaneously with mass transfer data, unlike the Raman spectroscopy method presented in Deleau et al. (2020). This colorimetric method can be applied to any aqueous system that can be acidified with carbon dioxide and therefore offers a means to investigate the underground geological carbon capture processes, whereby salt water is acidified by carbon dioxide at high-pressure conditions. The methodology developed in this study can also be easily adapted for for any other gas–liquid systems where mass transfer is observable with a color change.

The colorimetric method developed in this study has been applied to the flow and mass transfer in a H_2O-CO_2 system at 10 MPa and 303 K. The values obtained for the volumetric mass transfer coefficient were in the range 1 s^{-1} to 13 s^{-1}, which are in agreement with the study by Deleau et al. (2020) for similar conditions. It was observed that the volumetric mass transfer coefficient k_La_L decreases along the capillary tube and for the operating conditions studied here, it was found that k_La_L is 2.5 to 4 times higher in the bubble generation zone, compared with at the end of the tube. It has been shown that the higher value of k_La_L in the bubble generation zone is due to an increase in the specific surface area a_L available for mass transfer, but more specifically an increase in k_L. This increase in k_L is explained by the changing velocity gradients due to the transient nature of the bubble generation process. It was also found that k_La_L increases with increasing gas-to-liquid volumetric flow rate ratio and this increase was shown to be solely due to an increase in a_L.

In comparison with the Raman spectroscopy method presented in our previous work (Deleau et al., 2020), the equipment and materials used in the method presented here are less expensive and more accessible. On the other hand, the calibration of pH with greyscale, the image analysis and the fine-tuning of optimal parameters (e.g. shutter opening, lighting power, BPB concentration, capillary diameter and operating conditions) is more time consuming compared with the Raman spectra processing method. The current colorimetric method also has the advantage of providing data on both mass transfer and the physical characteristics of the two-phase flow simultaneously, thereby enabling the impact of operating conditions on both k_L and a_L to be analysed separately.

CRediT authorship contribution statement

T. Deleau: Conceptualization, Data curation, Formal analysis, Investigation, Methodology, Writing – original draft. **J-J. Letourneau:** Conceptualization, Formal analysis, Supervision, Writing – review & editing, Funding acquisition. **S. Camy:** Conceptualization, Supervision, Writing – review & editing, Funding acquisition. **J. Aubin:** Conceptualization, Supervision, Writing – review & editing, Funding acquisition. **F. Espitalier:** Conceptualization, Supervision, Writing – review & editing, Funding acquisition.

Declaration of Competing Interest

The authors declare that they have no known competing financial interests or personal relationships that could have appeared to influence the work reported in this paper.

Acknowledgements

The project leading to this result has received funding from the Occitanie region (France), MUSYS project (ALDOCT-000149-2017001788).

Appendix A. Operating conditions

Table A1

Table A1
Operating conditions employed during the experimental campaign at 10 MPa and 303 K.

$\dot{V}_{H_2O}$	$\dot{V}_{CO_2}$	U_L	U_F	Re_L	Re_F	$10^4 Ca_L$	$10^5 Ca_F$	U_{TP}	U_B	$\frac{\dot{V}_{CO_2}}{\dot{V}_{H_2O}}$
		$\frac{\dot{V}_{H_2O}}{S}$	$\frac{\dot{V}_{H_2O}}{S}$	$\frac{\rho_L U_L D}{\mu_L}$	$\frac{\rho_F U_F D}{\mu_F}$	$\frac{U_L \mu_L}{\sigma}$	$\frac{U_F \mu_F}{\sigma}$	$U_L + U_F$		
μL·min^{-1}	μL·min^{-1}	cm·s^{-1}	cm·s^{-1}	–	–	–	–	cm·s^{-1}	cm·s^{-1}	–
150	58.9	5.1	1.7	15.9	49.5	14	3.8	6.8	7	0.33
200	58.9	6.8	1.7	21.3	49.5	18	3.8	8.5	9	0.25
250	58.9	8.5	1.7	26.6	49.5	23	3.8	10.2	11	0.20
300	58.9	10.2	1.7	31.9	49.5	27	3.8	11.9	12	0.17
350	76.6	11.9	2.2	37.2	64.3	32	4.9	14.1	15	0.19
350	94.2	11.9	2.7	37.2	79.2	32	6.0	14.6	16	0.23
350	111.9	11.9	3.2	37.2	94.0	32	7.1	15.1	17	0.27
110	82.5	3.7	2.4	11.7	69.3	10	5.3	6.1	7	0.64
150	82.5	5.1	2.4	15.9	69.3	14	5.3	7.5	8	0.47
200	82.5	6.8	2.4	21.3	69.3	18	5.3	9.2	10	0.35
300	82.5	10.2	2.4	31.9	69.3	27	5.3	12.6	14	0.23

Appendix B. Derivation of the expression for mass transfer using the unit-cell model

Considering a finite volume of the H_2O-rich slug, the partial molar balance of CO_2 can be written as Equation (B.1) where C_{CO_2} is the concentration of CO_2 in the liquid volume and $\boldsymbol{N_{CO_2}}$ the combined molar flux (convective and diffusive) of CO_2 passing through the surface of this volume.

$$\frac{\partial C_{CO_2}}{\partial t} = -\nabla \cdot \boldsymbol{N_{CO_2}} \tag{B.1}$$

Equation (B.1) is integrated over the entire volume of the H_2O-rich slug, V_L:

$$\iiint_{V_L} \frac{\partial C_{CO_2}}{\partial t} dV = -\iiint_{V_L} \nabla \cdot \boldsymbol{N_{CO_2}} dV \tag{B.2}$$

Using the Green-Ostrogradski theorem, the right term is written as a flux passing through the boundary of volume V_L, i.e. the surface S_L, which is decomposed into S_b, S_{in}, S_{out} and S_{cap}

$$-\iiint_{V_L} \nabla \cdot \boldsymbol{N_{CO_2}} dV = -\iint_{S_L} \boldsymbol{N_{CO_2}} \cdot \boldsymbol{n} dS$$
$$= -\iint_{S_b} \boldsymbol{N^b_{CO_2}} \cdot \boldsymbol{n_b} dS - \iint_{S_{in}} \boldsymbol{N^{in}_{CO_2}} \cdot \boldsymbol{n_{in}} dS$$
$$-\iint_{S_{out}} \boldsymbol{N^{out}_{CO_2}} \cdot \boldsymbol{n_{out}} dS - \iint_{S_{cap}} \boldsymbol{N^{cap}_{CO_2}} \cdot \boldsymbol{n_{cap}} dS \tag{B.3}$$

The integral on S_{cap} is zero since there is no transfer through the capillary tube wall. The integrals on S_{in} and S_{out} are determined by considering a random cross-sectional surface S in the liquid slug that is moving with the mean flow velocity (Lagrangian approach), and the total flux through this surface is written by Equation (B.4):

$$\iint_S \boldsymbol{N_{CO_2}} \cdot \boldsymbol{n} dS \tag{B.4}$$

This total flux is non-zero even in a Lagrangian approach since the concentration of CO_2 in the liquid phase at the end of the capillary is higher than the concentration at the inlet. Considering the surfaces before and after this surface S, spaced by one unit-cell (like S_{in} and S_{out}), it is reasonable to say that if the surfaces are far enough from the bubble generation zone, the total flux through these surfaces are almost equal. Applying this argument to the surfaces S_{in} and S_{out} of the unit-cell, the integral on S_{in} and S_{out} are removed from Equation (B.3) since they are negligible compared with the integral on S_{cap}. The validity of this hypothesis can be altered if the length of the liquid slug is significantly greater than the length of the gas bubble (which is at least one order of magnitude higher) or if the variation of the liquid mixture density along the capillary due to CO_2 dissolution in the liquid phase is too high since it modifies the convective term of the total flux. For the CO_2-H_2O system, this hypothesis is valid and it gives Equation (B.5):

$$-\iint_{S_L} \boldsymbol{N_{CO_2}} \cdot \boldsymbol{n} dS = -\iint_{S_b} \boldsymbol{N^b_{CO_2}} \cdot \boldsymbol{n_b} dS \tag{B.5}$$

The total flux can be written using the global liquid mass transfer coefficient K_L. Furthermore, since H_2O is almost insoluble in the CO_2-rich phase, the global liquid mass transfer coefficient is equal to the liquid local mass transfer coefficient k_L. It gives Equation (B.6) where S_b is the bubble surface,$C^*_{CO_2}$ the concentration of CO_2 in the H_2O-rich slug when the thermodynamic equilibrium is reached and $\langle C_{CO_2} \rangle$ the mean concentration in the liquid slug volume V_L:

$$-\iint_{S_b} \boldsymbol{N^b_{CO_2}} \cdot \boldsymbol{n_b} dS = -\iint_{S_b} N^b_{CO_2}(-\boldsymbol{n_b}) \cdot \boldsymbol{n_b} dS$$
$$= k_L(C^*_{CO_2} - \langle C_{CO_2} \rangle) S_b \tag{B.6}$$

The left term of Equation (B.2) is decomposed using the Leibnitz theorem where $\boldsymbol{v_s}$ is the velocity vector of the moving surface S_L:

$$\iiint_{V_L} \frac{\partial C_{CO_2}}{\partial t} dV = \frac{d}{dt} \iiint_{V_L} C_{CO_2} dV - \iint_{S_L} C_{CO_2} \boldsymbol{v_s} \cdot \boldsymbol{n} dS \tag{B.7}$$

The first term of Equation (B.7) is decomposed in Equation (B.8):

$$\frac{d}{dt} \iiint_{V_L} C_{CO_2} dV = \langle C_{CO_2} \rangle \frac{dV_L}{dt} + V_L \frac{d\langle C_{CO_2} \rangle}{dt} \tag{B.8}$$

The second term of Equation (B.7) is separated with the four contributions of S_L in Equation (B.9):

$$-\iint_{S_L} C_{CO_2} \boldsymbol{v_s} \cdot \boldsymbol{n} dS = -\iint_{S_{in}} C_{CO_2} \boldsymbol{v_{in}} \cdot \boldsymbol{n_{in}} dS - \iint_{S_b} C_{CO_2} \boldsymbol{v_b} \cdot \boldsymbol{n_b} dS$$
$$-\iint_{S_{out}} C_{CO_2} \boldsymbol{v_{out}} \cdot \boldsymbol{n_{out}} dS - \iint_{S_{cap}} C_{CO_2} \boldsymbol{v_{cap}} \cdot \boldsymbol{n_{cap}} dS \tag{B.9}$$

The term on S_{cap} is zero since the velocity of the surface $\boldsymbol{v_{cap}}$ is zero. The terms on S_{in} and S_{out} are calculated by assuming that the mean concentrations on both surfaces are equal to the mean concentration in the entire liquid slug V_L (this assumption is not valid for long liquid slugs or near the bubble generation zone). The term V_{UC} corresponds to the entire unit-cell volume $V_L + V_B$:

$$-\iint_{S_{in}} C_{CO_2} \boldsymbol{v_{in}} \cdot \boldsymbol{n_{in}} dS - \iint_{S_{out}} C_{CO_2} \boldsymbol{v_{out}} \cdot \boldsymbol{n_{out}} dS$$
$$= -\langle C_{CO_2} \rangle \frac{dV_{UC}}{dt} \tag{B.10}$$

The term S_b is calculated by assuming that the concentration at the bubble interface is uniform over the entire bubble surface and equal to the concentration at equilibrium $C^*_{CO_2}$. Moreover, it is assumed that the velocity vector $\boldsymbol{v_b}$ is collinear to the bubble normal vector $\boldsymbol{n_b}$. The validity of these assumptions can be altered when the bubble has a non spherical shape (Silva, 2014) or when the surface tension is not constant over the entire surface (i.e. Marangoni effect).

$$-\iint_{S_b} C_{CO_2} \boldsymbol{v_b} \cdot \boldsymbol{n_b} dS = C^*_{CO_2} \frac{dV_b}{dt} \tag{B.11}$$

Equations (B.6), (B.8), (B.10) and (B.11) are substituted into Equation (B.2) and to give Equation (B.12) :

$$V_L \frac{d\langle C_{CO_2} \rangle}{dt} + (C^*_{CO_2} - \langle C_{CO_2} \rangle) \frac{dV_b}{dt} = k_L (C^*_{CO_2} - \langle C_{CO_2} \rangle) S_b \tag{B.12}$$

The term $(C^*_{CO_2} - \langle C_{CO_2} \rangle) \frac{dV_b}{dt}$ is only neglected when the variation of the bubble size is not significant (which is the case in the CO_2-H_2O system). Equation (B.13) is then obtained with $a_L = \frac{S_b}{V_L}$ the specific surface:

$$\frac{d\langle C_{CO_2} \rangle}{dt} = k_L a_L (C^*_{CO_2} - \langle C_{CO_2} \rangle) \tag{B.13}$$

The Lagrangian approach enables the time derivative to be converted into a spatial derivative by assuming that the unit-cell model is moving at the mean velocity U_{TP}:

$$\frac{d\langle C_{CO_2} \rangle}{dz} = \frac{k_L a_L}{U_{TP}} (C^*_{CO_2} - \langle C_{CO_2} \rangle) \tag{B.14}$$

Finally, $k_L a_L$ is extracted and it gives Equation (1).

Appendix C. Uncertainty calculations

The uncertainty calculation on the CO_2 concentrations in the colorimetric method is performed with the following steps. For

fixed operating conditions, all the greyscale values of all the measurement spots are standardized ((value-average)/standard deviation) and a normal distribution test is performed. The result is presented in Fig. C.1. It can be seen that the greyscale standardized distribution is not scattered and follows a normal law.

A Monte Carlo statistical method is applied at a fixed position along the axis of the capillary tube and a random draw of 1000 values are taken from the distribution of the greyscales. For each greyscale value obtained, a random draw in the corresponding possible pH values from the calibration curve is performed. This method allows to take into account the uncertainty in the calibration curve. An example is given In Fig. C.2, which presents the pH distribution obtained at z = 33.7 mm for the experiment at 10 MPa, 303 K where $\dot{V}_{CO_2}$ = 58.9 μLmin^{-1}, $\dot{V}_{H_2O}$ = 150 μLmin^{-1}.

The standard deviation of the pH distribution in Fig. C.2 is equal to 0.036. The same analysis has been performed for 100 values of axial positions that are linearly spaced between z = 0 and z = 18.9 cm. The maximum standard deviation obtained was 0.15; this value was in the bubble generation zone. This method provides uncertainty on the pH values obtained. However, since the CO_2 concentrations are interpolated with experimental values from Peng et al. (2013), it is not possible to give an uncertainty on the CO_2 concentrations in the H_2O-rich phase. Nevertheless, average errors on the CO_2 concentration filtered curves obtained with the Fast Fourier Transform of discrete values were calculated and the average error (square root of the sum of the square residuals between the experimental and filtered curves) did not exeed 5%.

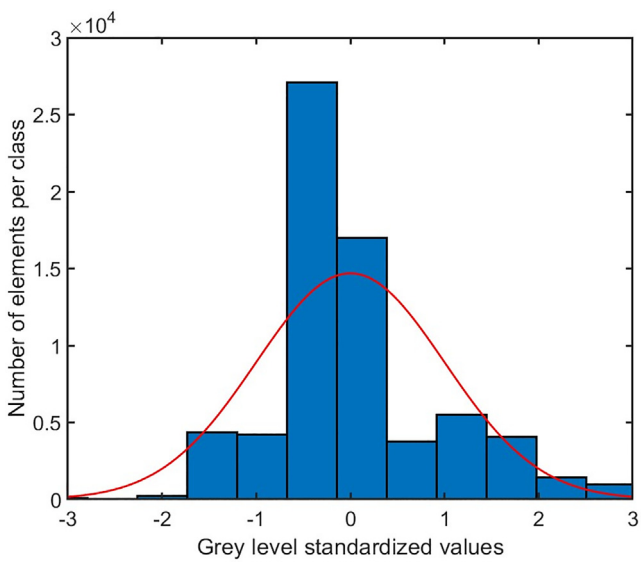

Fig. C1. Standardized class distribution of greyscale values of all the measurement spots at 10 MPa, 303 K, $\dot{V}_{CO_2}$ = 58.9 μL·min^{-1} and $\dot{V}_{H_2O}$ = 150 μL·min^{-1}.

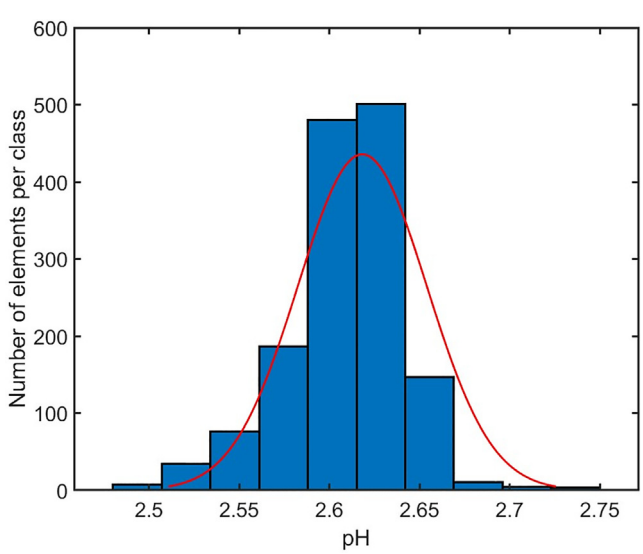

Fig. C2. pH class distribution at z = 33.7 cm, 10 MPa, 303 K, $\dot{V}_{CO_2}$ = 58.9 μL·min^{-1} and $\dot{V}_{H_2O}$ = 150 μL·min^{-1}.

References

Abolhasani, M., Kumacheva, E., Günther, A., 2015. Peclet Number Dependence of Mass Transfer in Microscale Segmented Gas Liquid Flow. Ind. Eng. Chem. Res. 54 (36), 9046–9051. https://doi.org/10.1021/acs.iecr.5b01991.

Abuzar, S.M., Hyun, S.-M., Kim, J.-H., Park, H.J., Kim, M.-S., Park, J.-S., Hwang, S.-J., 2018. Enhancing the Solubility and Bioavailability of Poorly Water-Soluble Drugs Using Supercritical Antisolvent (SAS) Process. Int. J. Pharm. 538 (1), 1–13. https://doi.org/10.1016/j.ijpharm.2017.12.041.

Akbar, M.K., Plummer, D.A., Ghiaasiaan, S.M., 2002. « Gas-Liquid Two-Phase Flow Regimes in Microchannels ». Janvier 527–534. https://doi.org/10.1115/IMECE2002-39555.

Andersson, M., Rodriguez-Meizoso, I., Turner, C., Hjort, K., Klintberg, L., 2018. Dynamic pH determination at high pressure of aqueous additive mixtures in contact with dense CO2. J. Supercrit. Fluids 136 (juin), 95–101. https://doi.org/10.1016/j.supflu.2018.02.012.

Arora, D., Sedev, R., Beh, C.C., Priest, C., Foster, N.R., 2020. Precipitation of Drug Particles Using a Gas Antisolvent Process on a High-Pressure Microfluidic Platform. Ind. Eng. Chem. Res. 59 (25), 11905–11913. https://doi.org/10.1021/acs.iecr.0c01484.

Assmann, N., Kaiser, S., Rudolf, P., von Rohr, 2012. Supercritical extraction of vanillin in a microfluidic device. J. Supercrit. Fluids 67 (juillet), 149–154. https://doi.org/10.1016/j.supflu.2012.03.015.

van Baten, J.M., Krishna, R., 2004. CFD simulations of mass transfer from Taylor bubbles rising in circular capillaries. Chem. Eng. Sci. 59 (12), 2535–2545. https://doi.org/10.1016/j.ces.2004.03.010.

Blanch-Ojea, R., Tiggelaar, R.M., Pallares, J., Grau, F.X., Gardeniers, J.G.E., 2012. Flow of CO2-ethanol and of CO2-methanol in a non-adiabatic microfluidic T-junction at high pressures. Microfluid. Nanofluid. 12 (6), 927–940. https://doi.org/10.1007/s10404-011-0927-x.

Bretherton, F.P., 1961. The motion of long bubbles in tubes. J. Fluid Mech. 10 (2), 166–188. https://doi.org/10.1017/S0022112061000160.

Campos Domínguez, Candela, Gamse, Thomas, 2016. Process intensification by the use of micro devices for liquid fractionation with supercritical carbon dioxide. Chem. Eng. Res. Des. 108 (avril), 139–145. https://doi.org/10.1016/j.cherd.2016.01.011. The 15th European Conference on Mixing.

Cheng, Yu-Shen, Pei-Min, Lu., Huang, Chun-Yin, Jia-Jiuan, Wu., 2017. Encapsulation of Lycopene with Lecithin and α-Tocopherol by Supercritical Antisolvent Process for Stability Enhancement. J. Supercrit. Fluids 130 (décembre), 246–252. https://doi.org/10.1016/j.supflu.2016.12.021.

Conde-Hernández, Lilia A., Espinosa-Victoria, José R., Trejo, Arturo, Guerrero-Beltrán, José Á., 2017. CO2-Supercritical Extraction, Hydrodistillation and Steam Distillation of Essential Oil of Rosemary (Rosmarinus Officinalis). J. Food Eng. 200 (mai), 81–86. https://doi.org/10.1016/j.jfoodeng.2016.12.022.

DaSilva, Jimmy Oliveira, Lehnherr, Dan, Liu, Jinchu, Bennett, Raffeal, Haidar, Imad A., Ahmad, Michael Hicks, Mann, Benjamin F., DiRocco, Daniel Adam, Regalado, Erik L., 2020. Generic Enhanced Sub/Supercritical Fluid Chromatography: Blueprint for Highly Productive and Sustainable Separation of Primary Hindered Amines. ACS Sustain. Chem. Eng. 8 (15), 6011–6021. https://doi.org/10.1021/acssuschemeng.0c00777.

Deleau, T., Fechter, M.H.H., Letourneau, J.-J., Camy, S., Aubin, J., Braeuer, A.S., Espitalier, F., 2020. Determination of mass transfer coefficients in high-pressure two-phase flows in capillaries using Raman spectroscopy. Chem. Eng. Sci. 228, (décembre). https://doi.org/10.1016/j.ces.2020.115960 115960.

Dietrich, N., Loubière, K., Jimenez, M., Hébrard, G., Gourdon, C., 2013. A new direct technique for visualizing and measuring gas–liquid mass transfer around bubbles moving in a straight millimetric square channel. Chem. Eng. Sci. 100 (août), 172–182. https://doi.org/10.1016/j.ces.2013.03.041. 11th International Conference on Gas-Liquid and Gas-Liquid-Solid Reactor Engineering.

Eskin, Dmitry, Mostowfi, Farshid, 2012. A model of a bubble train flow accompanied with mass transfer through a long microchannel. Int. J. Heat Fluid Flow 33 (1), 147–155. https://doi.org/10.1016/j.ijheatfluidflow.2011.11.001.

Ganapathy, H., Shooshtari, A., Dessiatoun, S., Alshehhi, M., Ohadi, M., 2014. Fluid flow and mass transfer characteristics of enhanced CO2 capture in a minichannel reactor. Appl. Energy 119 (avril), 43–56. https://doi.org/10.1016/j.apenergy.2013.12.047.

Garstecki, Piotr, Fuerstman, Michael J., Stone, Howard A., Whitesides, George M., 2006. Formation of droplets and bubbles in a microfluidic T-junction–scaling and mechanism of break-up. Lab Chip 6 (3), 437–446. https://doi.org/10.1039/B510841A.

Gavoille, Theo, Pannacci, Nicolas, Bergeot, Ghislain, Marliere, Claire, Marre, Samuel, 2019. Microfluidic approaches for accessing thermophysical properties of fluid systems. React. Chem. Eng. 4 (10), 1721–1739. https://doi.org/10.1039/C9RE00130A.

Gupta, Raghvendra, Fletcher, David F., Haynes, Brian S., 2009. On the CFD modelling of Taylor flow in microchannels. Chem. Eng. Sci. 64 (12), 2941–2950. https://doi.org/10.1016/j.ces.2009.03.018.

Haase, Stefan, Murzin, Dmitry Yu., Salmi, Tapio, 2016. Review on hydrodynamics and mass transfer in minichannel wall reactors with gas–liquid Taylor flow. Chem. Eng. Res. Des. 113 (septembre), 304–329. https://doi.org/10.1016/j.cherd.2016.06.017.

Jaouhari, T., Zhang, F., Tassaing, T., Fery-Forgues, S., Aymonier, C., Marre, S., Erriguible, A., 2020. Process intensification for the synthesis of ultra-small organic nanoparticles with supercritical CO2 in a microfluidic system. Chem. Eng. J. 397, (octobre). https://doi.org/10.1016/j.cej.2020.125333 125333.

Klima, Tobias C., Braeuer, Andreas S., 2019. Vapor-liquid-equilibria of fuel-nitrogen systems at engine-like conditions measured with Raman spectroscopy in micro capillaries. Fuel 238 (février), 312–319. https://doi.org/10.1016/j.fuel.2018.10.108.

Kuhn, Simon, Jensen, Klavs F., 2012. A pH-Sensitive Laser-Induced Fluorescence Technique To Monitor Mass Transfer in Multiphase Flows in Microfluidic Devices. Ind. Eng. Chem. Res. 51 (26), 8999–9006. https://doi.org/10.1021/ie300978n.

Labauze, Hélène, Camy, Séverine, Floquet, Pascal, Benjelloun-Mlayah, Bouchra, Condoret, Jean-Stéphane, 2018. Kinetic Study of 5-Hydroxymethylfurfural Synthesis from Fructose in High Pressure CO 2 –Water Two-Phase System. Ind. Eng. Chem. Res. 58 (1), 92–100. https://doi.org/10.1021/acs.iecr.8b04694.

Lefortier, Stéphanie G.R., Hamersma, Peter J., Bardow, André, Kreutzer, Michiel T., 2012. Rapid microfluidic screening of CO2 solubility and diffusion in pure and mixed solvents. Lab on a Chip 12 (18), 3387–3391. https://doi.org/10.1039/C2LC40260B.

Liu, N., Aymonier, C., Lecoutre, C., Garrabos, Y., Marre, S., 2012. Microfluidic approach for studying CO2 solubility in water and brine using confocal Raman spectroscopy. Chem. Phys. Lett. 551 (novembre), 139–143. https://doi.org/10.1016/j.cplett.2012.09.007.

Liu, Yanyan, Zhao, Qiankun, Yue, Jun, Yao, Chaoqun, Chen, Guangwen, 2021. Effect of Mixing on Mass Transfer Characterization in Continuous Slugs and Dispersed Droplets in Biphasic Slug Flow Microreactors. Chem. Eng. J. 406, (février). https://doi.org/10.1016/j.cej.2020.126885 126885.

Luther, Sebastian K., Schuster, Julian J., Leipertz, Alfred, Braeuer, Andreas, 2013. Microfluidic investigation into mass transfer in compressible multi-phase systems composed of oil, water and carbon dioxide at elevated pressure. J. Supercrit. Fluids 84 (décembre), 121–131. https://doi.org/10.1016/j.supflu.2013.10.002.

Macedo Portela da Silva, Nayane, Letourneau, Jean-Jacques, Espitalier, Fabienne, Prat, Laurent, 2014. Transparent and Inexpensive Microfluidic Device for Two-Phase Flow Systems with High-Pressure Performance. Chem. Eng. Technol. 37 (11), 1929–1937.

Marre, S., Aymonier, C., Subra, P., Mignard, E., 2009. Dripping to jetting transitions observed from supercritical fluid in liquid microcoflows. Appl. Phys. Lett. 95 (13), 134105. https://doi.org/10.1063/1.3242375.

Marre, Samuel, Adamo, Andrea, Basak, Soubir, Aymonier, Cyril, Jensen, Klavs F., 2010. Design and Packaging of Microreactors for High Pressure and High Temperature Applications. Ind. Eng. Chem. Res. 49 (22), 11310–11320. https://doi.org/10.1021/ie101346u.

Martin, Alexandre, Camy, Séverine, Aubin, Joëlle, 2018. Hydrodynamics of CO2-ethanol flow in a microchannel under elevated pressure. Chem. Eng. Sci. 178 (mars), 297–311. https://doi.org/10.1016/j.ces.2017.12.046.

Martin, Alexandre, Teychené, Sébastien, Camy, Séverine, Aubin, Joëlle, 2016. Fast and inexpensive method for the fabrication of transparent pressure-resistant microfluidic chips. Microfluid. Nanofluid. 20 (6), 92. https://doi.org/10.1007/s10404-016-1757-7.

Ou, Zhisong, Jin, Hui, Ren, Zhenhua, Zhu, Shixing, Song, Mengmeng, Guo, Liejin, 2019. Mathematical Model for Coal Conversion in Supercritical Water: Reacting Multiphase Flow with Conjugate Heat Transfer. Int. J. Hydrogen Energy 44(30). 15746–15757. https://doi.org/10.1016/j.ijhydene.2018.09.139. Special issue based on the papers selected from the International Conference on Clean Energy 2017.

Peng, Cheng, Crawshaw, John P., Maitland, Geoffrey C., Martin Trusler, J.P., Vega-Maza, David, 2013. The pH of CO2-saturated water at temperatures between 308K and 423K at pressures up to 15MPa. J. Supercrit. Fluids 82 (octobre), 129–137. https://doi.org/10.1016/j.supflu.2013.07.001.

Peters, Christine, Wolff, Ludger, Haase, Sandra, Thien, Julia, Brands, Thorsten, Koß, Hans-Jürgen, Bardow, André, 2017. Multicomponent diffusion coefficients from microfluidics using Raman microspectroscopy. Lab Chip 17 (16), 2768–2776. https://doi.org/10.1039/C7LC00433H.

Quitain, Armando T., Mission, Elaine G., Sumigawa, Yoshifumi, Sasaki, Mitsuru, 2018. Supercritical carbon dioxide-mediated esterification in a microfluidic reactor. Chem. Eng. Process. Process Intensif. 123 (janvier), 168–173. https://doi.org/10.1016/j.cep.2017.11.002.

Ren, Jian, He, Songbo, Ye, Chunbo, Chen, Guangwen, Sun, Chenglin, 2012. The ozone mass transfer characteristics and ozonation of pentachlorophenol in a novel microchannel reactor. Chem. Eng. J. 210 (novembre), 374–384. https://doi.org/10.1016/j.cej.2012.09.011.

Roy, Daipayan, Farooq Wahab, M., Talebi, Mohsen, Armstrong, Daniel W., 2020. Replacing Methanol with Azeotropic Ethanol as the Co-Solvent for Improved Chiral Separations with Supercritical Fluid Chromatography (SFC). Green Chem. 22 (4), 1249–1257. https://doi.org/10.1039/C9GC04207E.

Sattari-Najafabadi, Mehdi, Esfahany, Mohsen Nasr, Zan, Wu., Sunden, Bengt, 2018. Mass transfer between phases in microchannels: A review. Chem. Eng. Process. Process Intensif. 127 (mai), 213–237. https://doi.org/10.1016/j.cep.2018.03.012.

Silva, Nayane Macedo Portela da, 2014. Développement d'un système micro/millifluidique sous pression pour l'étude et la mesure de propriétés d'écoulement diphasique: application au binaire CO2 supercritique - BMimPF6. Phdthesis, Ecole des Mines d'Albi-Carmaux. https://tel.archives-ouvertes.fr/tel-01079222/document.

van Steijn, Volkert, Kreutzer, Michiel T., Kleijn, Chris R., 2007. micro-PIV study of the formation of segmented flow in microfluidic T-junctions. Chem. Eng. Sci. 62 (24), 7505–7514. https://doi.org/10.1016/j.ces.2007.08.068. 8th International Conference on Gas-Liquid and Gas-Liquid-Solid Reactor Engineering.

Tan, J., Lu, Y.C., Xu, J.H., Luo, G.S., 2012. Mass transfer characteristic in the formation stage of gas–liquid segmented flow in microchannel. Chem. Eng. J. 185–186 (mars), 314–320. https://doi.org/10.1016/j.cej.2012.01.054.

Toews, Karen L., Shroll, Robert M., Wai, Chien M., Smart, Neil G., 1995. pH-Defining Equilibrium between Water and Supercritical CO2. Influence on SFE of Organics and Metal Chelates. Anal. Chem. 67 (22), 4040–4043. https://doi.org/10.1021/ac00118a002.

Triplett, K.A., Ghiaasiaan, S.M., Abdel-Khalik, S.I., Sadowski, D.L., 1999. Gas–liquid two-phase flow in microchannels Part I: two-phase flow patterns. Int. J. Multiph. Flow 25 (3), 377–394. https://doi.org/10.1016/S0301-9322(98)00054-8.

Vandu, C.O., Liu, H., Krishna, R., 2005. Mass transfer from Taylor bubbles rising in single capillaries. Chem. Eng. Sci. 60 (22), 6430–6437. https://doi.org/10.1016/j.ces.2005.01.037. 7th International Conference on Gas-Liquid and Gas-Liquid-Solid Reactor Engineering.

Verboom, W., 2009. Selected Examples of High-Pressure Reactions in Glass Microreactors. Chem. Eng. Technol. 32 (11), 1695–1701. https://doi.org/10.1002/ceat.200900369.

Völkel, Norbert, 2009. Design and characterization of gas-liquid microreactors. Phdthesis. http://ethesisinp-toulouse.fr/archive/00001061/.

Waelchli, Severin, Rudolf von Rohr, Philipp, 2006. Two-phase flow characteristics in gas–liquid microreactors. Int. J. Multiph. Flow 32 (7), 791–806. https://doi.org/10.1016/j.ijmultiphaseflow.2006.02.014.

Yao, Chaoqun, Dong, Zhengya, Zhao, Yuchao, Chen, Guangwen, 2014. An online method to measure mass transfer of slug flow in a microchannel. Chem. Eng. Sci. 112 (juin), 15–24. https://doi.org/10.1016/j.ces.2014.03.016.

Yao, Chaoqun, Zhu, Kai, Liu, Yanyan, Liu, Hongchen, Jiao, Fengjun, Chen, Guangwen, 2017. Intensified CO2 absorption in a microchannel reactor under elevated pressures. Chem. Eng. J. 319 (juillet), 179–190. https://doi.org/10.1016/j.cej.2017.03.003.

Yousefi, Mohammad, Rahimi-Nasrabadi, Mehdi, Pourmortazavi, Seied Mahdi, Wysokowski, Marcin, Jesionowski, Teofil, Ehrlich, Hermann, Mirsadeghi, Somayeh, 2019. Supercritical Fluid Extraction of Essential Oils. TrAC Trends Analyt. Chem. 118 (septembre), 182–193. https://doi.org/10.1016/j.trac.2019.05.038.

Yue, Jun, Chen, Guangwen, Yuan, Quan, Luo, Lingai, Gonthier, Yves, 2007. Hydrodynamics and mass transfer characteristics in gas–liquid flow through a rectangular microchannel. Chem. Eng. Sci. 62 (7), 2096–2108. https://doi.org/10.1016/j.ces.2006.12.057.

Zhang, Peng, Yao, Chaoqun, Ma, Haiyun, Jin, Nan, Zhang, Xunli, Lü, Hongying, Zhao, Yuchao, 2018. Dynamic changes in gas-liquid mass transfer during Taylor flow in long serpentine square microchannels. Chem. Eng. Sci. 182 (juin), 17–27. https://doi.org/10.1016/j.ces.2018.02.018.

Zhao, Qiankun, Ma, Haiyun, Liu, Yanyan, Yao, Chaoqun, Yang, Lixia, Chen, Guangwen, 2021. Hydrodynamics and Mass Transfer of Taylor Bubbles Flowing in Non-Newtonian Fluids in a Microchannel. Chem. Eng. Sci. 231, (février). https://doi.org/10.1016/j.ces.2020.116299 116299.